

**Fano resonances in the optical scattering force upon a high-index dielectric nanoparticle**Xiao-Yong Duan<sup>1,2</sup> and Zhi-Guo Wang<sup>1,\*</sup><sup>1</sup>*School of Physics Science and Engineering, Tongji University, Shanghai 200092, China*<sup>2</sup>*School of Mathematics, Physics and Information Engineering, Jiaying University, Jiaying 314001, China*

(Received 6 July 2017; published 6 November 2017)

Effects of Fano resonances on optical scattering force upon a high-index dielectric nanoparticle radiated by a plane wave are theoretically investigated. The results demonstrate that five different types of Fano resonances appear in the force and are expressed in a unified way. The magnetic (electric) -based cascades of Fano resonances dominate the peaks of the force. The magnetic (electric) -based conventional Fano resonances and the unconventional Fano resonances suppress the peaks of the force for particular large nanoparticles. All types of Fano resonances together cause broad dips of the force and even a near-zero force effect at particular radii. Finally, by investigating the effects of positive and negative indexes, loss, and gain of the particle on the force, it is shown that negative force arises only as the appropriate gain is introduced in the particle. Our results are important for not only deep understanding of electromagnetic interactions in the optical force but also stable optical manipulation of the dielectric nanoparticle.

DOI: [10.1103/PhysRevA.96.053811](https://doi.org/10.1103/PhysRevA.96.053811)**I. INTRODUCTION**

The optical force as an important tool for contactless micromanipulation of micro- and nano-scale objects has attracted great attention [1–3]. In general, the optical force takes the form of the optical scattering force (OSF) or radiation pressure, optical intensity or phase-gradient force, and optical binding force in different situations. On one hand, the OSF is utilized to levitate [4] and accelerate [5] micron-sized particles due to the transferred momentum from light to particle. On the other hand, the optical intensity-gradient force emerging from the inhomogeneous light field is employed to trap steadily nanoparticle at the position where the field intensity is at a maximum [2]. Additionally, the optical phase-gradient force coming from the phase gradient of the Gaussian beam is used to drive the assembly of the silver (Ag) nanoparticles and transform its structure from a one-dimensional chain to two-dimensional lattices [6]. Analogously, the optical binding force, which results from the multiple scattering of the plane electromagnetic (EM) wave among particles, can be explored to organize micron-sized polystyrene spheres into several stable and quasistable geometric configurations [7] and assemble Ag nanoparticle into chains, arrays, and clusters [8].

As mentioned above, the optical force comes from the light-matter interactions. The theoretical result [9] showed further that the interference phenomena emerge in the OSF on the magnetodielectric particle. The interferences are caused by the interactions of the incident fields and scattered fields reradiated by the induced electric and magnetic dipoles in the particle. What is fascinating is that the Fano resonances (FRs) may appear in the force and affect it because of the interferences between a narrow discrete resonance and a broad continuous mode [10].

For the metal nanoparticle, the FRs are mainly caused by the electric effect because the metal hardly has a magnetic response to the incident light in the optical spectrum due to the absence of the field inside the particle [11]. When a Gaussian

beam radiates a homogeneous Ag or gold (Au) nanosphere deviated from the beam axis, the FR resulting from the electric dipole-quadrupole interference gives rise to a transverse OSF. The force is perpendicular to the incident wave vector and pulls or pushes the particle into or out of the beam axis depending on the particle radius and incident wavelength [12]. For instance, the transverse OSF can push the phase-change nanoparticle Ge<sub>2</sub>Sb<sub>2</sub>Te<sub>5</sub>-Au core-shell with “amorphous” and “crystalline” structural states and small biomolecules to opposite directions [13,14]. In addition, by utilizing the zero-order Bessel beam to illuminate the homogeneous Au, Au-Ag core-shell, and hollow Ag shell particles pinned on the beam axis, the FRs coming from the electric dipole-quadrupole and quadrupole-octupole interferences can tailor the longitudinal OSF along the incident direction and even induce a pulling force [15]. Under illumination of a Gaussian evanescent wave, the direction of the vertical component of the OSF, which is perpendicular to prism-air interface, on a Ag nanoparticle can be repeatedly reversed [16]. It is caused by the multipolar FRs arising from the adjacent two-order electric multipole moments.

Unlike the metal, the FRs in dielectric nanoparticle possess rich types based on the electric, magnetic, and electric-magnetic coupling effects [17]. The effects result from the induced electric and magnetic multipole moments due to the oscillations of the induced charges and displacement currents inside the particle excited by incident light [11]. The individual Mie scattering coefficient (MSC) of the high-index nanorod [18] and nanosphere [19,20] is regarded as the interference between the narrow Mie scattering mode excited in the particle and the broad background. Therefore, the MSCs can be expressed as an infinite series of FRs in terms of the cascades of FRs wherein the each resonance is a conventional FR [21]. Additionally, the FR also can be caused by the interference between the adjacent (or same) order multipole moments with the same (or different) EM mode(s) excited in the particle. The former is known as conventional FR [10] contributed by the electric or magnetic dipole-quadrupole, quadrupole-octupole, octupole-hexadecapole interferences, etc. The latter is called unconventional FR caused by the electric-magnetic dipole, quadrupole, octupole, hexadecapole interferences, etc.

\*zgwang@tongji.edu.cn

[22–24]. Recently the dielectric nanoparticle with low loss and rich electric and magnetic responses has been regarded as a potential replacement for metal nanoparticles in the manufacture of optically resonant nanostructures, which has attracted more attention [17]. Therefore, the optical manipulation will be widely applied in assembly of dielectric nanostructures. Nevertheless, the uniform expressions of the various types of FRs and their effects on the OSF upon a dielectric nanoparticle have not been investigated to the best of our knowledge. This is a fundamental physical question, and it is important to modulate the optical force in optical manipulation of the dielectric nanoparticle.

In this theoretical paper, our results demonstrate explicitly and generally that the OSF, which is caused by a linearly polarized plane EM wave, on a dielectric nanoparticle can be decomposed into five components. The components show individually the different types of FRs with diverse physical mechanisms. Importantly, we offer a unified way to express the different types of FRs in the OSF and investigate the effects of the FRs on the peaks and dips of the OSF. Finally, by changing the refractive index of the particle, the results show that the negative OSF arises only for the particle with appropriate gain under illumination of the plane EM wave.

The paper is arranged as follows. In Sec. II the OSF is decomposed into five components based on the different types of FRs. The physical mechanisms of the various types of the FRs in the OSF components are individually disclosed. The uniform expressions of the different types of FRs are offered in the OSF. The positions of the OSF's peaks and dips are analytically derived based on the FR's conditions of the scattered field. In Sec. III the effects of the different types of the multipolar FRs on the OSF are numerically investigated in detail. In Sec. IV the effects of the refractive index of the particle on OSF are discussed. Finally, in Sec. V a brief summary and conclusions are presented.

## II. UNIFIED EXPRESSION OF DIVERSE FRs IN OSF

In light-matter interaction, the momentum transfer from light to particle, resulting from the scattering and/or absorption of photons caused by particle, exerts force on the particle along the direction of the beam propagation, called OSF (or radiation pressure). On one hand, the momentum absorbed by particle per unit time is  $I_0 C_{\text{abs}}/c$  because of momentum = energy/ $c$ , where  $I_0$  is the intensity of beam in units of  $\text{W}/\text{m}^2$ ,  $C_{\text{abs}}$  is the absorption cross section of particle in units of  $\text{m}^2$ , and  $c$  is the speed of light in vacuum. On the other hand, the photons impinging particle are elastically scattered with different scattering angle  $\theta$ , and the net momentum transfer to the direction of propagation per unit time caused by the scattering is  $I_0 C_{\text{sca}}(1 - \langle \cos\theta \rangle)/c$ . Here  $C_{\text{sca}}$  is scattering cross section and  $\langle \cos\theta \rangle$  is asymmetry parameter defined as the average cosine of the scattering angle. Therefore the total momentum transfer to the particle per unit time, called OSF,  $F = I_0(C_{\text{ext}} - C_{\text{sca}}\langle \cos\theta \rangle)/c$ , where  $C_{\text{ext}}$  is extinction cross section and  $C_{\text{ext}} = C_{\text{sca}} + C_{\text{abs}}$  based on the law of conservation of energy. For distinguishing different types of light-matter interactions, the OSF on a dielectric nanosphere caused by a linearly polarized plane EM wave [25] is

expanded as

$$F = F_{M'} + F_{E'} + F_{M'M'+1} + F_{E'E'+1} + F_{E'M'}. \quad (1)$$

Among them,

$$F_{M'} = A \sum_l (2l+1) \text{Re}(b_l), \quad (2)$$

$$F_{E'} = A \sum_l (2l+1) \text{Re}(a_l), \quad (3)$$

$$F_{M'M'+1} = -A \sum_l \frac{2l(l+2)}{l+1} \text{Re}(b_l b_{l+1}^*), \quad (4)$$

$$F_{E'E'+1} = -A \sum_l \frac{2l(l+2)}{l+1} \text{Re}(a_l a_{l+1}^*), \quad (5)$$

$$F_{E'M'} = -A \sum_l \frac{2(2l+1)}{l(l+1)} \text{Re}(a_l b_l^*), \quad (6)$$

where  $A = 2\pi I_0 n_m / k^2 c$  and  $I_0 = n_m \varepsilon_0 c |E_0|^2 / 2$  [28];  $E_0$  is the electric intensity of the incident wave with time-dependent factor  $\exp(-i\omega t)$  and angular frequency  $\omega$  in a medium;  $\varepsilon_0$  is the permittivity of vacuum;  $k = 2\pi n_m / \lambda$  is the wave vector in a surrounding medium with refractive index  $n_m$ ;  $\lambda$  is the incident wavelength in vacuum;  $a_l$  and  $b_l$  are the MSCs characterizing, respectively, the scattered electric and magnetic fields (for analytic expressions see Ref. [26]); the reduced sum  $\sum_l$  represents the summation of  $l$  from 1 to  $\infty$ ; the star means complex conjugate; and  $\text{Re}(x)$  indicates the real part of  $x$ . The optical gradient force vanishes because of the unchanged field intensity of the plane wave.

The OSF is explicitly decomposed into five components in Eq. (1), which exhibit respectively different types of interferences between the light fields [27]. What is amazing is that each of the interferences can be represented in the forms of the multipolar FRs with different types as shown by Eqs. (2)–(6). The term  $F_{M'}$  ( $F_{E'}$ ) in Eq. (2) [Eq. (3)] is caused by the interference between the scattered fields re-emitted by the magnetic (electric) multipole moments excited in the particle and the incident field. It is presented through the magnetic (electric) -based cascade of FRs of the individual magnetic (electric) MSCs  $b_l(a_l)$ , which results from the interference between the narrow magnetic (electric) multipole moments in the particle and the broad background [21]. In the physical point of view, the two force components  $F_{M'}$  and  $F_{E'}$ , termed incident force, are caused by the momentums transferred from light to particle and are positive directing to the incident wave vector. They denote the interaction between the scattered and incident fields and play leading roles in the OSF as explained in Sec. III. The term  $F_{M'M'+1}$  ( $F_{E'E'+1}$ ) in Eq. (4) [Eq. (5)] comes from the interference between the scattered fields re-emitted by the adjacent-order magnetic (electric) multipole moments  $b_l$  and  $b_{l+1}$  ( $a_l$  and  $a_{l+1}$ ). It is represented as the magnetic (electric)-based conventional FRs as shown by the term  $b_l b_{l+1}^*$  ( $a_l a_{l+1}^*$ ) [10]. The term  $F_{E'M'}$  in Eq. (6) results from the interference between the scattered fields reradiated by the same-order electric and magnetic multipole moments such as  $a_l$  and  $b_l$ . It is presented by the unconventional FRs as shown by the term  $a_l b_l^*$  [22]. The last three terms in Eq. (1), named recoil force, demonstrating the interactions between

the scattered fields, may be positive or negative at different particle radii. In despite of their small contributions on the OSF comparing with the first two terms in Eq. (1), they display rich physical mechanisms of the electric and/or magnetic interactions and can suppress the OSF's peak at particular large radius as discussed in Sec. III. What is unexpected is that the diverse FRs with different physical mechanisms appear simultaneously in the same OSF system and are expressed in a unified way. It exhibits the rich physics in the optical properties of the dielectric nanoparticle.

In general, the incident force overcomes the recoil force and dominates the OSF. Consequently, it is necessary to investigate analytically the effects of the cascades of FRs of MSCs  $a_l$  and  $b_l$ , arising in the incident force, on the extrema of the OSF. To this end, it is convenient to write the Mie coefficients in the alternative forms [10,28]

$$\begin{aligned} a_l &= \frac{F_l^{(a)}}{F_l^{(a)} + iG_l^{(a)}}, & b_l &= \frac{F_l^{(b)}}{F_l^{(b)} + iG_l^{(b)}}, \\ c_l &= \frac{in}{F_l^{(b)} + iG_l^{(b)}}, & d_l &= \frac{in}{F_l^{(a)} + iG_l^{(a)}}, \end{aligned} \quad (7)$$

where  $F_l^{(a)}, G_l^{(a)}, F_l^{(b)}$ , and  $G_l^{(b)}$  are auxiliary functions depending on  $n$  and  $x$  (for analytic expressions see Ref. [20]); the relative refractive index  $n = n_p/n_m$  represents the ratio of the refractive index of particle ( $n_p$ ) to that of the environment medium ( $n_m$ ); and  $x = kR$  and  $R$  stand for the size parameter and radius of the sphere, respectively. For the lossless material with real refractive index, the auxiliary functions are real functions. The internal coefficients  $d_l$  and  $c_l$  represent, respectively, the internal electric and magnetic fields inside the particle. It is clear from Eq. (7) that the points at  $|a_l| = 1$  and  $|b_l| = 1$  correspond, respectively, to the electric and magnetic resonances (constructive interference) of the scattered fields whose positions are determined by  $G_l^{(a),(b)}(n, x) = 0$ . On the other hand, the points at  $|a_l| = 0$  and  $|b_l| = 0$  correspond individually to the electric and magnetic antiresonances (destructive interference) of the scattered fields whose positions are defined by  $F_l^{(a),(b)}(n, x) = 0$ .

At the high refractive index limit, Tribelsky and Miroschnichenko [20] have derived the refractive index ( $n$ ) formulas satisfying the conditions of the FRs of the  $a_l$  and  $b_l$  in the case of fixed  $R$  and  $\lambda$ . But from the experimental point of view, it is rather easy to change the radius of the nanoparticle and hardly to change the refractive index of material. Therefore, we derive the particle radius ( $R$ ) formulas [Eqs. (8)–(11)] fulfilling the resonance and anti-resonance of the  $a_l$  and  $b_l$  by fixing  $n_p, n_m$ , and  $\lambda$ . Here based on the analogous strategy in Ref. [20], we first derive the size parameter  $\tilde{x}^{(E),(H)}$  at the resonant points of the internal coefficients  $d_l$  and  $c_l$ , after that expand  $F_l^{(a),(b)}$  and  $G_l^{(a),(b)}$  in the vicinity of the resonant points, and then obtain the small departure of the size parameter  $\delta x$  from  $\tilde{x}^{(E),(H)}$  satisfying the resonant and antiresonant conditions of  $a_l$  and  $b_l$ . Last, based on the relations  $x = \delta x + \tilde{x}^{(E)}$ ,  $x = \tilde{x}^{(H)} - \delta x$ , and  $R = x/k$ , we give the particle radius formulas at the resonant and antiresonant points of the  $a_l$  and  $b_l$ . The advantage of this method is that it can avoid the uncertainty of the type 0/0 brought by the direct calculations of the resonances of  $a_l$  and  $b_l$ . It is noteworthy that the resonant peaks of  $|b_l|$  shift to

blue with respect to  $|c_l|$ , which is contrary to that the resonant peaks of  $|a_l|$  shift to red with respect to  $|d_l|$  as shown by Fig. 9 in the Appendix. Therefore, we choose backward difference  $\delta x = \tilde{x}^{(H)} - x$  for the resonance of the scattered magnetic field, which is contrary to the forward difference adopted in the scattered electric field.

The radii of the particle satisfy the resonance ( $|a_l| = 1$ ) and antiresonance ( $|a_l| = 0$ ) of the scattered electric field are respectively expressed as

$$R_G^{(a)} = (l + 2p) \frac{\lambda}{4n_p} + \frac{\lambda}{2\pi n_p n} \frac{\chi_l(\tilde{x}^{(E)})}{\chi_l'(\tilde{x}^{(E)})}, \quad (8)$$

$$R_F^{(a)} = (l + 2p) \frac{\lambda}{4n_p} + \frac{\lambda}{2\pi n_p n} \frac{\psi_l(\tilde{x}^{(E)})}{\psi_l'(\tilde{x}^{(E)})}, \quad (9)$$

where  $\psi_l(z) = zj_l(z)$  and  $\chi_l(z) = -zy_l(z)$  are Riccati-Bessel functions,  $j_l(z)$  and  $y_l(z)$  are, respectively, the spherical Bessel functions of the first and second kinds; the primes denote the derivative with respect to the entire argument  $z$ ; the recurrence relations of the derivatives are  $\psi_l'(z) = zj_{l-1}(z) - lj_l(z)$  and  $\chi_l'(z) = -zy_{l-1}(z) + ly_l(z)$ ;  $l$  is the order of the resonant multipole moment ( $l = 1, 2, 3, \dots$ ); and the non-negative integer  $p$  represents the frequency of each resonant multipole moment ( $p = 1, 2, 3, \dots$  for electric type and  $p = 0, 1, 2, \dots$  for magnetic type because the values must satisfy the high refractive index condition (Fraunhofer region) as  $n\tilde{x}^{(E),(H)} \geq 2l$  [20] for electric and magnetic resonances, respectively). The formula  $\tilde{x}^{(E)} = (l + 2p)\pi/(2n)$  determines the particular size parameter meeting the resonant condition of the internal coefficients ( $|d_l| = 1$ ).

The radii of the particle satisfying the resonance ( $|b_l| = 1$ ) and antiresonance ( $|b_l| = 0$ ) of the scattered magnetic field are individually determined by

$$R_G^{(b)} = (l + 2p + 1) \frac{\lambda}{4n_p} + \frac{\lambda}{2\pi n_p n} \frac{\chi_l'(\tilde{x}^{(H)})}{\chi_l(\tilde{x}^{(H)})}, \quad (10)$$

$$R_F^{(b)} = (l + 2p + 1) \frac{\lambda}{4n_p} + \frac{\lambda}{2\pi n_p n} \frac{\psi_l'(\tilde{x}^{(H)})}{\psi_l(\tilde{x}^{(H)})}. \quad (11)$$

The formula  $\tilde{x}^{(H)} = (l + 2p + 1)\pi/(2n)$  determines the particular size parameter meeting the resonant condition of the internal coefficients ( $|c_l| = 1$ ). Note that Eqs. (10) and (11) also satisfy the condition  $n\tilde{x} \geq 2l$  for the high refractive index limit. The  $x$  should be carefully chosen to avoid the singular points which are caused by the functions  $\psi_l(x)$ ,  $\chi_l(x)$ , and their derivatives in the denominators in Eqs. (8)–(11).

### III. RESULTS

Let us consider a lossless silicon nanosphere with refractive index  $n_p = 4$  in a visible spectrum [29] embedded in nonabsorptive water ( $n_m = 1.33$ ) [15] and illuminated by a linearly polarized plane EM wave. The incident wavelength is  $\lambda = 532$  nm in a range of visible spectrum in vacuum, and the intensity is  $I_0 = 10$  mW/ $\mu\text{m}^2$ .

#### A. Effects of the multipolar FRs with different types on OSF

The OSF (as shown in Fig. 1) is decomposed into five components  $F_{M^l}, F_{E^l}, F_{M^l M^{l+1}}, F_{E^l E^{l+1}}$ , and  $F_{E^l M^l}$  as shown by

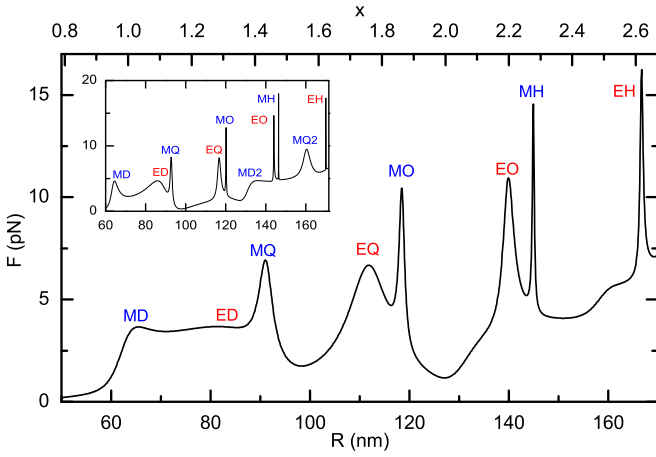


FIG. 1. The OSF in units of pN upon a spherical silicon nanoparticle with refractive index  $n_p = 4$  in water with refractive index  $n_m = 1.33$  illuminated by a linearly polarized plane EM wave ( $\lambda = 532$  nm in vacuum) as a function of the particle radius ( $R$ ). The radius ranges from 50 to 170 nm (bottom axis), and the corresponding size parameter ( $x$ ) ranges from 0.79 to 2.67 (upper axis). MD, MQ, MO, and MH (ED, EQ, EO, and EH) denote individually the peaks of the OSF, which are mainly caused by the magnetic (electric)-based cascades of FRs of the MD, MQ, MO, and MH (ED, EQ, EO, and EH) corresponding to  $l = 1, 2, 3$ , and 4. The insert shows the OSF at the same condition, but the particle is embedded in air with refractive index  $n_{\text{air}} = 1$ . The MD2 and MQ2 denote the second FRs of the MD and MQ.

the black solid curves (right axis as indicated by the black arrows) in Figs. 2–6. The OSF is mainly dominated by the incident force  $F_{M^i}$  and  $F_{E^i}$  (see black solid curves in Figs. 1–3), which originate from the interference between the scattered and incident fields. The force component  $F_{M^i}$  in Eq. (2) is presented by the magnetic-based cascades of FRs of the  $b_l$  as shown by the black solid curve in Fig. 2. Magnetic dipole (MD) first arises in the case of small particle, while the real part of the first-order magnetic MSC reaches the maximum value  $\text{Re}(b_1) = 1$  as shown by the red dash-dot-dotted curve in Fig. 2 where the radius of the particle  $R = 64$  nm. Bearing in mind that we use  $\text{Re}(b_l)$  and  $\text{Re}(a_l)$  to analyze the FR instead of  $|b_l|^2$  and  $|a_l|^2$  employed in the previous research [20]. The reasons are that the terms  $b_l$  and  $a_l$  appear in the OSF as shown in Eqs. (2)–(6) and the relations both  $\text{Re}(b_l) = |b_l|^2$  and  $\text{Re}(a_l) = |a_l|^2$  are tenable for nonabsorptive particle [28]. The  $F_{M^i}$  (marked by “MD” in Figs. 1 and 2) arrives at the local maximum value at the same position as seen from the black solid curve in Fig. 2. The peak is caused by the MD-FR ( $l = 1$ ), which is induced by the interference between the re-emitted fields by the MD excited in the particle and the background. With the increase of the particle radius, the magnetic quadrupole (MQ) occurs when  $\text{Re}(b_2) = 1$  at the  $R = 91$  nm as shown by the blue dashed curve in Fig. 2 as well as the force arrives at the peak denoted by “MQ” in Figs. 1 and 2. The peak is dominated by the MQ-FR ( $l = 2$ ), which is induced by the interference between the re-emitted fields by the MQ and the background. When the particle radius increases further, a magnetic octupole (MO) and hexadecapole (MH) appear successively when  $\text{Re}(b_3) = 1$  and  $\text{Re}(b_4) = 1$  at

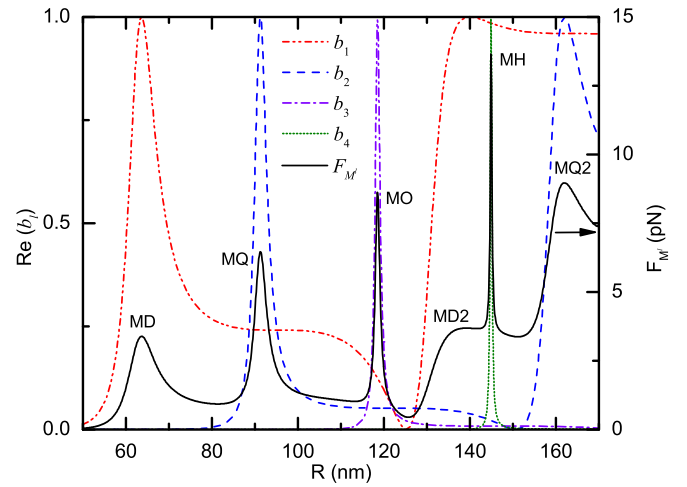


FIG. 2. The real parts of four magnetic MSCs  $b_1$  (red dash-dot-dotted curve),  $b_2$  (blue dashed curve),  $b_3$  (purple dash-dotted curve), and  $b_4$  (green dotted curve), calculated by the rigorous Mie scattering theory, as functions of the particle radius ( $R$ ) (left axis). The force component  $F_{M^i}$  is shown by the black solid curve (right axis as denoted by the black arrow). The peaks of the force denoted by MD, MQ, MO, and MH correspond, respectively, to the magnetic-based cascades of FRs of the MD, MQ, MO, and MH at the radius  $R = 64, 91, 119$ , and  $145$  nm. The other two peaks denoted by MD2 and MQ2 correspond, respectively, to the second FRs of the MD and MQ at the radius  $R = 139$  and  $162$  nm.

$R = 119$  and  $145$  nm as shown by the purple dash-dotted and green dotted curves in Fig. 2, respectively. The force reaches individually the peaks as shown by MO and MH in Figs. 1 and 2. The two peaks are respectively dominated by the MO-FR ( $l = 3$ ) and MH-FR ( $l = 4$ ), which are induced by the interferences between the re-emitted fields by the individual MO and MH and the background.

The analogous phenomena are also found in the force component  $F_{E^i}$  in Eq. (3) represented by the electric-based cascades of FRs, which are induced by the interference between the electric multipole moments and the background. The electric dipole (ED), quadrupole (EQ), octupole (EO), and hexadecapole (EH) arise in order when  $\text{Re}(a_l) = 1$  for  $l = 1, 2, 3$ , and 4 with the increase of the particle size. The resonant positions respond to radii  $R = 84, 112, 140$ , and  $167$  nm, respectively, as shown by the red dash-dot-dotted, blue dashed, purple dash-dotted, and green dotted curves in Fig. 3. At the positions, the peaks of  $F_{E^i}$  also emerge synchronously as seen from the black solid curve in Fig. 3. The peaks are respectively dominated by the ED-FR ( $l = 1$ ), EQ-FR ( $l = 2$ ), EO-FR ( $l = 3$ ), and EH-FR ( $l = 4$ ) due to the interferences between the scattered fields re-emitted by the individual ED, EQ, EO, and EH and the background as shown by ED, EQ, EO, and EH in Figs. 1 and 3.

Because of the cascades of FRs, the MD, MQ, and ED responses in the particle achieve respectively the second FR. The resonant position of the former responds to  $R = 139$  nm and that of the latter two responds to  $R = 162$  nm. It is clearly seen from that the real parts of the  $b_1, b_2$ , and  $a_1$  reach the maximum again as shown by the red dash-dot-dotted and blue dashed curves in Fig. 2 and the red dash-dot-dotted curve in

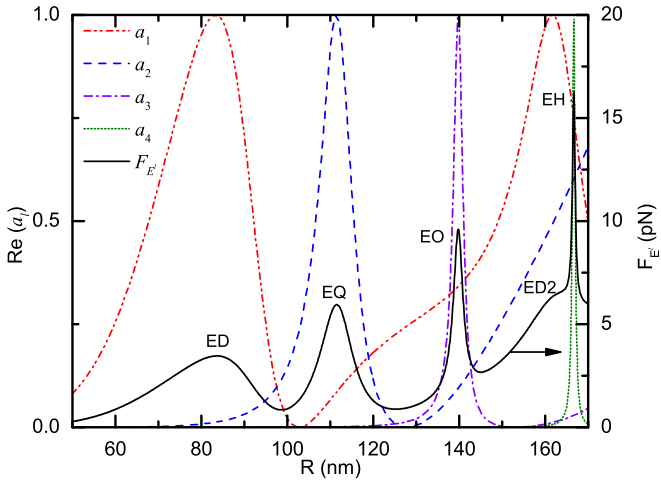


FIG. 3. The real parts of four electric MSCs  $a_1$  (red dash-dotted curve),  $a_2$  (blue dashed curve),  $a_3$  (purple dash-dotted curve), and  $a_4$  (green dotted curve), calculated by the rigorous Mie scattering theory, as functions of the particle radius ( $R$ ) (left axis). The force component  $F_{E^l}$  is shown by the black solid curve (right axis as denoted by the black arrow). The peaks of the force denoted by ED, EQ, EO, and EH correspond respectively to the electric-based cascades of FRs of the ED, EQ, EO, and EH at the radius  $R = 84, 112, 140,$  and  $167$  nm. The peak denoted by ED2 corresponds to the second FR of the ED at the radius  $R = 162$  nm.

Fig. 3. Consequently, the second ED-FR and MQ-FR cause respectively a small shoulder in  $F_{E^l}$  and a second peak in  $F_{M^l}$  at the same position  $R = 162$  nm as shown by ED2 in Fig. 3 and MQ2 in Fig. 2. Additionally, the second MD-FR gives rise to a broad shoulder in  $F_{M^l}$  at  $R = 139$  nm denoted by MD2 in Fig. 2. In general, the magnetic- and electric-based multiple cascades of FRs dominate the peaks of the OSF.

The force component  $F_{M^l M^{l+1}}$  ( $F_{E^l E^{l+1}}$ ) in Eq. (4) [Eq. (5)] is induced by the interference between the scattered fields reradiated by the adjacent two-order magnetic (electric) multipole moments. Notably, the dips are indeed the peaks of the  $F_{M^l M^{l+1}}$ ,  $F_{E^l E^{l+1}}$ , and  $F_{E^l M^l}$  because of the negative sign in Eqs. (4)–(6). The peaks of the  $F_{M^l M^{l+1}}$  are represented by the magnetic-based conventional FRs such as magnetic dipole-quadrupole (MDQ) -FR, quadrupole-octupole (MQO) -FR, and octupole-hexadecapole (MOH) -FR. The three peaks correspond, respectively, to the resonances of the MDQ interference term  $\text{Re}(b_1 b_2^*) (l = 1)$ , MQO interference term  $\text{Re}(b_2 b_3^*) (l = 2)$ , and MOH interference term  $\text{Re}(b_3 b_4^*) (l = 3)$  in Eq. (4) as shown by the red dash-dot-dotted, blue dashed, and purple dotted curves in Fig. 4. The peaks of the OSF marked by MDQ, MQO, and MOH in Fig. 4 arise at the positions of the MQ, MO, and MH (marked by MQ, MO, and MH in Fig. 2). Interestingly, the second MDQ-FR leads to the largest peak in the force (marked by MDQ2 in Fig. 4) at the position of the second MQ (blue dashed curve in Fig. 2) because that the MD is nearly resonant at the same position (red dash-dot-dotted curve in Fig. 2). On the other hand, the peaks of the  $F_{E^l E^{l+1}}$  are contributed by the electric-based conventional FRs such as electric dipole-quadrupole (EDQ) -FR, quadrupole-octupole (EQO) -FR, and octupole-hexadecapole (EOH) -FR. The three peaks correspond respectively to the resonances of the EDQ

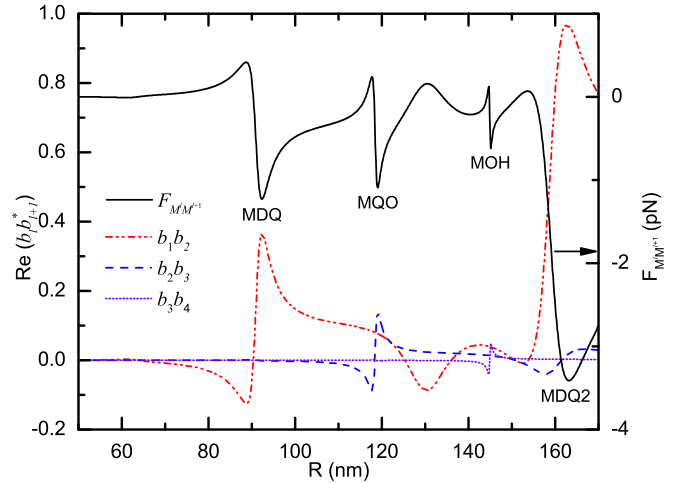


FIG. 4. The real parts of the terms  $b_1 b_2^*$  (red dashed-dot-dotted curve),  $b_2 b_3^*$  (blue dashed curve), and  $b_3 b_4^*$  (purple dotted curve), calculated by the rigorous Mie scattering theory, as functions of the particle radius ( $R$ ) (left axis). The force component  $F_{M^l M^{l+1}}$  is shown by the black solid curve (right axis as denoted by the black arrow). The peaks of the force denoted by MDQ, MQO, and MOH correspond, respectively, to the magnetic-based conventional FRs of the MDQ, MQO, and MOH. The last peak denoted by MDQ2 corresponding to the second FR of the MDQ arises at the position of the second FR of MQ.

interference term  $\text{Re}(a_1 a_2^*) (l = 1)$ , EQO interference term  $\text{Re}(a_2 a_3^*) (l = 2)$ , and EOH interference term  $\text{Re}(a_3 a_4^*) (l = 3)$  in Eq. (5) as shown by the red dash-dot-dotted, blue dashed, and purple dotted curves in Fig. 5. The peaks of the OSF marked

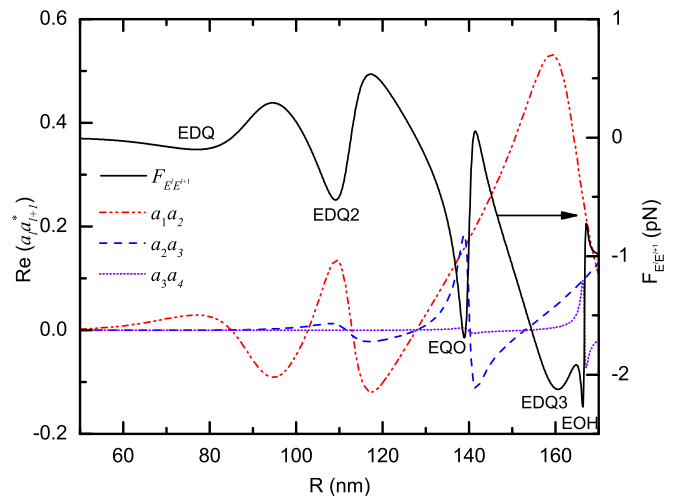


FIG. 5. The real parts of the terms  $a_1 a_2^*$  (red dashed-dot-dotted curve),  $a_2 a_3^*$  (blue dashed curve), and  $a_3 a_4^*$  (purple dotted curve), calculated by the rigorous Mie scattering theory, as functions of the particle radius ( $R$ ) (left axis). The force component  $F_{E^l E^{l+1}}$  is shown by the black solid curve (right axis as denoted by the black arrow). The peaks of the force denoted by EDQ, EQO, and EOH correspond, respectively, to the electric-based conventional FRs of the EDQ, EQO, and EOH. The peaks denoted by EDQ2 and EDQ3 corresponding, respectively, to the second and third FRs of the EDQ arise in the vicinity of the first EQ and at the position of the second ED.

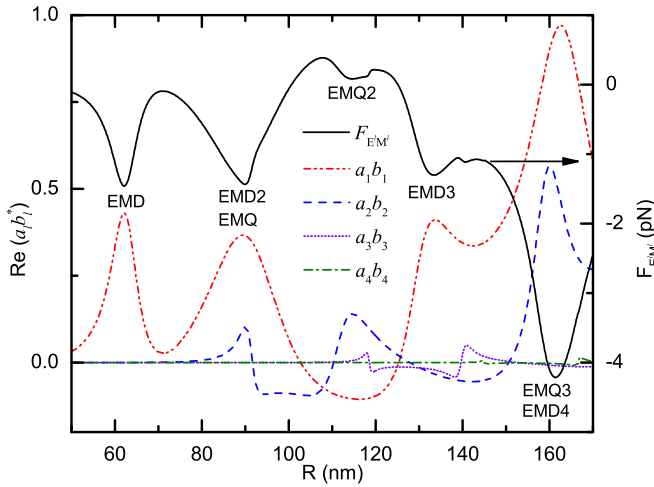


FIG. 6. The real parts of the  $a_1 b_1^*$  (red dash-dot-dotted curve),  $a_2 b_2^*$  (blue dashed curve),  $a_3 b_3^*$  (purple dotted curve), and  $a_4 b_4^*$  (green dash-dotted curve), calculated by the rigorous Mie scattering theory, as functions of the particle radius ( $R$ ) (left axis). The force component  $F_{E^l M^l}$  is shown by the black solid curve (right axis as denoted by the black arrow). The peaks of the force denoted by EMD, EMD2, EMD3, and EMD4 correspond, respectively, to the first, second, third, and fourth unconventional FRs of the EMD. The peaks of the force denoted by EMQ, EMQ2, and EMQ3 correspond, respectively, to the first, second, and third unconventional FRs of the EMQ. The peak marked by EMD arises in the vicinity of the first MD. The peak marked by EMD2 and EMQ arises in the vicinity of the first MQ. The peak marked by EMQ2 arises in the vicinity of the second EQ. The peak marked by EMD3 arises in the vicinity of the second MD. The peak marked by EMQ3 and EMD4 arises at the position of the second MQ.

by EDQ, EQO, and EOH in Fig. 5 arise at the positions of the EQ, EO, and EH (marked by EQ, EO, and EH in Fig. 3). As is the same as the magnetic type discussed above, the second and third EDQ-FRs also cause peaks in the force (marked by EDQ2 and EDQ3 in Fig. 5) at the positions of the first EQ and second ED (blue dashed and red dash-dot-dotted curves in Fig. 3). The two peaks are larger than the one denoted by EDQ since the broader second and third overlaps of the ED and EQ (red dash-dot-dotted and blue dashed curves in Fig. 3).

The force component  $F_{E^l M^l}$  in Eq. (6) originates from the interference between the scattered fields reradiated by the same-order magnetic and electric multipole moments. The peaks of the force are presented by the unconventional FRs such as electric-magnetic dipole (EMD)-FR, quadrupole (EMQ)-FR, octupole (EMO)-FR, and hexadecapole (EMH)-FR. The four peaks correspond respectively to the resonances of the EMD interference term  $\text{Re}(a_1 b_1^*)$  ( $l = 1$ ), EMQ interference term  $\text{Re}(a_2 b_2^*)$  ( $l = 2$ ), EMO interference term  $\text{Re}(a_3 b_3^*)$  ( $l = 3$ ), and EMH interference term  $\text{Re}(a_4 b_4^*)$  ( $l = 4$ ) in Eq. (6). The force is shown by the black solid curve in Fig. 6. The EMD-FR-induced peak in the force (marked by EMD in Fig. 6) emerges in the vicinity of the MD due to the resonance of the term  $\text{Re}(a_1 b_1^*)$  (red dash-dot-dotted curve in Fig. 6) caused by the constructive interference between the sharp resonant MD and the broad off-resonant ED (red dash-dot-dotted curves in Figs. 2 and 3). With increase of the

particle size, the second EMD-FR and EMQ-FR-induced peak (marked by EMD2 and EMQ in Fig. 6) arises at the position of the MQ because of the simultaneous appearance of the second resonance of the term  $\text{Re}(a_1 b_1^*)$  (red dash-dot-dotted curve) and the first resonance of the term  $\text{Re}(a_2 b_2^*)$  (blue dashed curve), which comes from the constructive interference between the sharp resonant MQ and the broad off-resonant EQ (blue dashed curves in Figs. 2 and 3). But the second EMD-FR dominates the peak of the force as seen from the red dash-dot-dotted and blue dashed curves in Fig. 6. The EMO-FR induced peak (not marked) appears hardly at the point of the MO because of the small overlap of the sharp EO and MO resonances (purple dash-dotted curves in Figs. 2 and 3). Analogously, the EMH-FR-induced peak vanishes owing to the off-overlap of the sharper EH and MH resonances (green dotted curves in Figs. 2 and 3). The second EMQ-FR, which is dominated by the EQ, induces a small peak behind the EQ (marked by the EMQ2 in Fig. 6; see also blue dashed curves in Figs. 2 and 3). With the further increase of the particle radius, the third EMD-FR causes the peak of the force (black solid curve in Fig. 6) in front of the position of the MD resonance (red dash-dot-dotted curve in Fig. 2). Interestingly, the fourth EMD-FR dominated by the ED resonance and third EMQ-FR led by the MQ resonance induce together the biggest peak of the force at the position  $R = 161$  nm where the second ED and MD achieve simultaneously resonances marked by EMD4 and EMQ3 in Fig. 6. It is noteworthy that in spite of the small contributions of the  $F_{M^l M^{l+1}}$ ,  $F_{E^l E^{l+1}}$ , and  $F_{E^l M^l}$  on the peaks of the OSF, the recoil force can suppress the peak of the OSF at particular large radius. For instance, the peaks of the  $F_{M^l M^{l+1}}$ ,  $F_{E^l E^{l+1}}$ , and  $F_{E^l M^l}$  in the nearby  $R = 162$  nm (black solid curves in Figs. 4–6) offset nearly the peaks of the  $F_{M^l}$  and  $F_{E^l}$  (black solid curves in Figs. 2 and 3) and destroy the peak of the OSF (Fig. 1).

The angular dependence of the scattered irradiance uncovers straightforwardly the physical origins of the negative  $F_{M^l M^{l+1}}$ ,  $F_{E^l E^{l+1}}$ , and  $F_{E^l M^l}$ . The scattered irradiance is independent of the azimuthal angle. The range of the polar (scattering) angle  $\theta$  is chosen from  $0^\circ$  to  $180^\circ$  because the scattering diagrams are symmetric about the polar axis. The black solid arrow represents the incident wave vector ( $\mathbf{k}$ ) in Figs. 7(a)–7(c). As shown by the scattering diagrams at radii  $R = 92, 119, 145,$  and  $163$  nm in Fig. 7(a), the scattered lights are predominately scattered into the forward half circle, which is caused by the interference between the scattered magnetic fields, and leads to the negative  $F_{M^l M^{l+1}}$ . The radii correspond respectively to the negative peaks of the  $F_{M^l M^{l+1}}$  marked by EDQ, EDQ2, EQO, EDQ3, and EOH in Fig. 5. Analogously, the negative  $F_{E^l E^{l+1}}$  and  $F_{E^l M^l}$  also originate from the predominant forward scattering ( $\theta = 0^\circ$ ). But the scattered lights are respectively caused by the scattered electric field interference and scattered electric-magnetic field interference. The former can be clearly seen from the scattering diagrams at radii  $R = 77, 109, 139, 161,$  and  $166$  nm in Fig. 7(b), which correspond to the negative peaks of the  $F_{E^l E^{l+1}}$  marked by MDQ, MQO, MOH, and MDQ2 in Fig. 4, respectively. The latter can be understood with the help of the scattering diagrams at radii  $R = 62, 90, 115, 133,$  and  $161$  nm in Fig. 7(c), which correspond to the negative peaks of the  $F_{E^l M^l}$  marked by EMD, EMQ (EMD2), EMQ2, EMD3, and

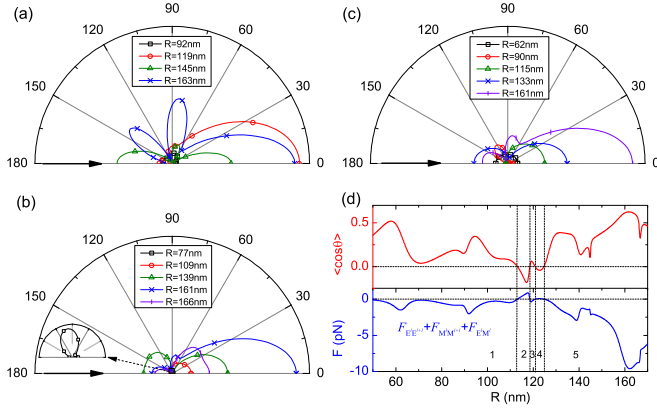


FIG. 7. Scattering properties and the component of the OSF  $F_{M^l M^{l+1}} + F_{E^l E^{l+1}} + F_{E^l M^l}$ . Scattering diagrams as functions of scattering angle for different particle radii and the black solid arrow denotes the wave vector ( $\mathbf{k}$ ) of the incident light (a)–(c). (a) Scattering diagrams at radii  $R = 92, 119, 145,$  and  $163$  nm corresponds respectively to the peaks of the  $F_{M^l M^{l+1}}$  marked by MDQ, MQO, MOH, and MDQ2 in Fig. 4. (b) Scattering diagrams at radii  $R = 77, 109, 139, 161,$  and  $166$  nm correspond, respectively, to the peaks of the  $F_{E^l E^{l+1}}$  marked by EDQ, EDQ2, EQO, EDQ3, and EOH in Fig. 5. Insert: Enlarged scattering diagram at  $R = 84$  nm (black curve). (c) Scattering diagrams at radii  $R = 62, 90, 115, 133,$  and  $161$  nm corresponds, respectively, to the peaks of the  $F_{E^l M^l}$  marked by EMD, EMQ (EMD2), EMQ2, EMD3, and EMQ4 (EMD4) in Fig. 6. (d) The asymmetry parameter  $\langle \cos\theta \rangle$  (red curve) and the component of the OSF  $F_{M^l M^{l+1}} + F_{E^l E^{l+1}} + F_{E^l M^l}$  (blue curve) as functions of  $R$ .

EMQ4 (EMD4) in Fig. 6, respectively. At radii  $R = 77$  nm [black curve with hollow square in the insert in Fig. 7(b)] and  $90$  nm [red curve with hollow circle in Fig. 7(c)], in spite of more scattering light falling into the backward half circle, the forward scattering surpasses the backward scattering ( $\theta = 180^\circ$ ) and results in negative forces  $F_{E^l E^{l+1}}$  and  $F_{E^l M^l}$ . The asymmetry parameter  $\langle \cos\theta \rangle$  [26] expresses weighted-average direction of the scattered radiation. It is positive in regions 1, 3, and 5 (red curve in Fig. 7(d)) and denotes that the particle scatters more light to the forward direction, which results in the negative force  $F_{M^l M^{l+1}} + F_{E^l E^{l+1}} + F_{E^l M^l}$  [blue curve in Fig. 7(d)]. On the contrary, the negative  $\langle \cos\theta \rangle$  in regions 2 and 4 demonstrates that the particle scatters more light to the backward direction, which causes the positive scattering force  $F_{M^l M^{l+1}} + F_{E^l E^{l+1}} + F_{E^l M^l}$ .

As expected, the resonance of the higher-order moment is induced in order in the particle with increase of the particle size, but its effect is smaller than that of the lower-order ones on the extinction (or scattering) efficiency [30]. However, the peak of the OSF contributed by the high-order FRs is dramatically

larger than that of the low-order ones as displayed in Fig. 1. The reason is that the extinction (or scattering) efficiency represents the ability of the particle to dissipate (or scatter) light per unit cross section, but the OSF is proportional to the surface area of the particle. Therefore, the effect of the high-order FR on the OSF is largely amplified in order with increase of the size of the particle.

### B. Positions of the OSF's peaks calculated by the FR of the scattered field

In Table I the radii of the particle at the peaks of the OSF are respectively calculated by the FR's conditions of the scattered field based on Eqs. (8) and (10) and a rigorous Mie solution. Due to the dominant contributions of the cascades of FRs on the OSF, the peaks of the OSF are mainly caused by the magnetic (electric) -based multipolar cascades of FRs, which are respectively represented by the MSCs  $b_1, b_2, b_3, b_4, b_{12},$  and  $b_{22}$  ( $a_1, a_2, a_3, a_4,$  and  $a_{12}$ ) as shown in Figs. 2 and 3. The terms  $b_{12}, b_{22},$  and  $a_{12}$  denote the second MD-FR, MQ-FR, and ED-FR. The peaks of the OSF calculated by the FR's conditions produce respectively small shifts relative to that calculated by the rigorous Mie solution because of the influences of the subordinate peaks, which come from the additional conventional and unconventional FRs, in the vicinity of the resonant positions (see the black solid curves in Figs. 4–6). The shift is quantitatively described by the ratio of the difference between the results of the FR's conditions and Mie solution to the result of the Mie solution. As shown in Table I, the shift enlarges with increase in the order of the multipole moment because that the effects of the higher-order conventional and unconventional FRs on the OSF increase when the radius of the particle is bigger than  $160$  nm (see the black curve in Fig. 1 and black solid curves in Figs. 4–6). But the relative uncertainty of the diameter of the actual nanoparticle manufactured in experiment is about  $8.6\%$  [6,8]. Therefore the peak values of the OSF on the high-index nanoparticle are well determined by the conditions of the FRs.

## IV. DISCUSSIONS OF THE EFFECTS OF REFRACTIVE INDEX ON OSF

The overlap of the broad ED-FR and MD-FR leads to a hardly changed OSF for small particle as shown by the flat part of the curve in Fig. 1. The reason is that the small relative refractive index ratio of  $n_p$  to  $n_m$  brings the broad ED and MD profile. On the contrary, with increase of the particle radius, the narrow high-order FR without spectral overlap arises in order and induces a sharp peak of the OSF at particular radius. The well-defined ED-FR and MD-FR-induced peak of the OSF can be produced through increasing the refractive

TABLE I. The radii (in units of nm) of the particle at the OSF's peaks calculated with the Mie solution and FR's conditions of the scattered field.

Term	$a_1$	$a_2$	$a_3$	$a_4$	$a_{12}$	$b_1$	$b_2$	$b_3$	$b_4$	$b_{12}$	$b_{22}$
Mie solution	83	111	140	167	162	64	91	119	145	140	162
FR's conditions	89	119	154	189	165	62	95	126	159	124	162
Shift of peak (%)	7.23	7.21	10.00	13.17	1.85	-3.13	4.40	5.88	9.67	-11.43	0

index ratio. For instance, putting the particle into medium with low refractive index such as air ( $n_{\text{air}} = 1$ ) as shown by MD and ED (the inset of Fig. 1). Additionally, the multipolar cascades of FRs cause higher and sharper peaks of the OSF in the condition of the higher ratio  $n_p/n_m$  as shown in the inset of Fig. 1. Surprisingly, a near-zero force effect with the minimum OSF 0.36 pN arises at the radius  $R = 97.6$  nm in the vicinity of the dip of cascade of the ED-FR. The effect can be utilized to design recoilless optical microscopy techniques [31]. The near-zero force effect seems to be a straightforward result of the condition  $F_z \approx 0$  when  $\langle \cos\theta \rangle \approx 1$  [26] which means that the incident and recoil forces offset nearly each other. But it can be achieved for high-index dielectric material such as silicon and germanium at some special points rather than the low-index dielectric material such as polystyrene. The physical mechanism “hidden” within the phenomenon refers to the excitations of the Mie eigenmodes in the particle, which is not clearly seen from the condition mentioned above. Under illumination of the beam, the multiple moments induced in the low-index particle have broad profiles with serious overlap. The dip of the dipole resonance, therefore, is easily superposed by the peaks of the higher-order moments (quadrupole, octupole, etc.). As a result, the near-zero force effect hardly arises because the local minima optical force results from the dip of the dipole is overlapped by the peaks

of the optical forces caused by the higher-order moments. On the contrary, the dips and peaks of the multiple moments in a high-index particle are more sharper and hardly overlap each other. Therefore, the high-index particle favors the near-zero force effect. On the other hand, the peak values of the OSF at some particular particle radii reach about 10–20 pN (see Fig. 1) and compare to or are even larger than the OSF on the metal nanoparticle with same order size. But the intensity of the incident light is  $I_0 = 10$  mW/ $\mu\text{m}^2$  in the paper and only a tenth of that needed by the metal nanoparticle [15]. It is advantageous to lower the need for laser power and reduce largely the heat effects of the laser and the thermal motion of the particle in optical trapping and manipulation.

FRs appear in OSF and influence significantly it for not only the lossless particle but also the particle with negative refractive index, loss, or gain. Figure 8 shows the OSFs on the spherical nanoparticles with real positive (a), real negative (b), complex refractive indexes with loss (c), and gain (d) in the same conditions in Fig. 1. The OSF on a particle with a higher refractive index possesses narrower peaks as shown in Fig. 8 (a) due to the sharper peaks of the FRs. The negative refractive index does not mean the negative OSF as shown in Fig. 8(b), which agrees with the previous report [32]. The dips of the FRs lead a minimum of the OSF, which does not reach zero and become negative. But they produce a near-zero force effect

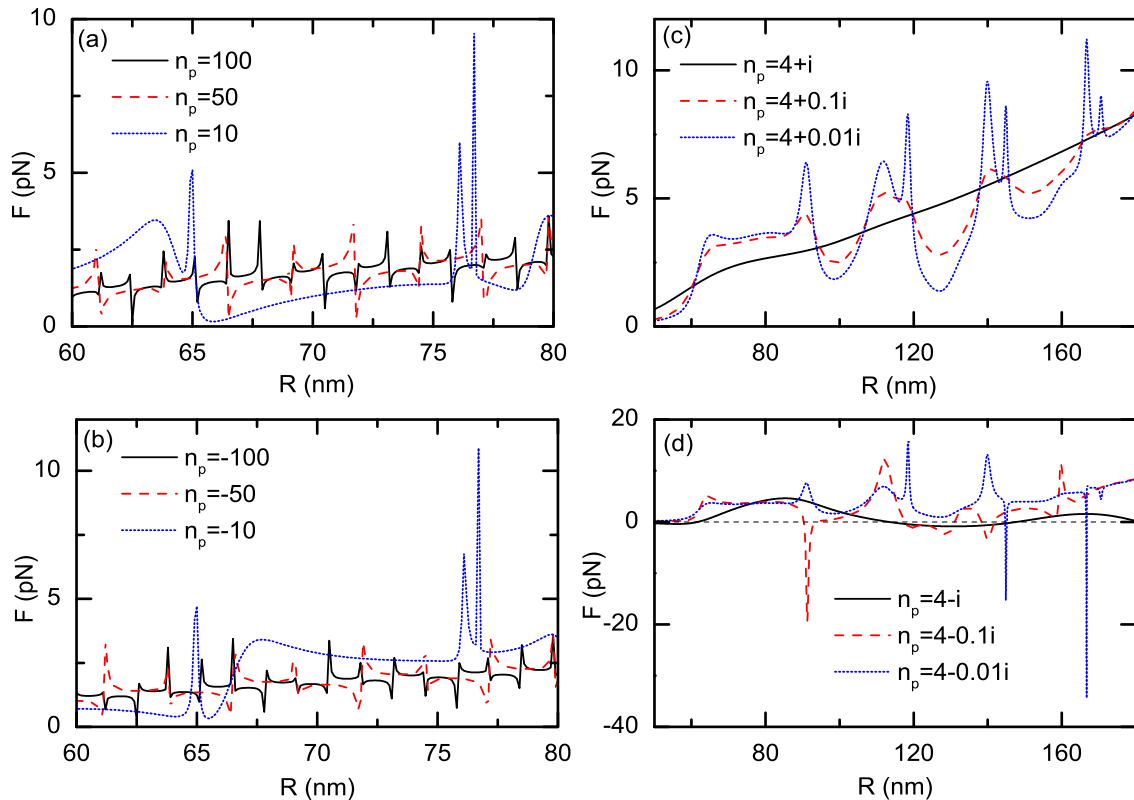


FIG. 8. The OSFs on spherical nanoparticle with different refractive index  $n_p$  in water ( $n_m = 1.33$ ) as a function of the particle radius ( $R$ ). The incident wavelength is  $\lambda = 532$  nm in vacuum. The radius of the particle ranges from 60 to 80 nm (a, b) and 50 to 180 nm (c, d). (a) Real positive index  $n_p = 100$  (black solid curve), 50 (red dashed curve), and 10 (blue dotted curve). (b) Real negative index  $n_p = -100$  (black solid curve),  $-50$  (red dashed curve), and  $-10$  (blue dotted curve). (c) Complex index with loss  $n_p = 4 + i$  (black solid curve),  $4 + 0.1i$  (red dashed curve), and  $4 + 0.01i$  (blue dotted curve). (d) Complex index with gain  $n_p = 4 - i$  (black solid curve),  $4 - 0.1i$  (red dashed curve), and  $4 - 0.01i$  (blue dotted curve).

at particular radii for the real positive and negative refractive index as shown in Figs. 8(a) and 8(b), which is similar to the lossless nanoparticle in air as shown in the insert of Fig. 1. For the lossy particle, a small loss benefits the occurrence of the peaks of the OSF as shown by the blue dotted curve in Fig. 8(c). But the large loss reduces (red dashed curve) and even suppresses completely (black solid curve) the peak of the OSF in Fig. 8(c). If we modulate the particle refractive index, it is the only possibility to realize the negative OSF (optical pulling force) by introducing gain into the particle [Fig. 8(d)], which agrees with the previous reports [33,34]. It is clear from the expression  $F_z = F_z^I + F_z^R$  in Ref. [15] because that the positive incident force  $F_z^I$  surpasses always the recoil force  $F_z^R$  and thus leads to a positive OSF  $F_z$  for the particle without gain. The aim of the introduction of the gain is to realize the negative extinction cross section  $\sigma_{\text{ext}}$  which is proportional to  $F_z^I$ . But the “possibility” means that the gain is a necessary conditions rather than a sufficient conditions for the negative OSF. Hence, it is interesting that how much gain can cause the negative OSF and how the gain excites the Fano resonances. Figure 8(d) demonstrates that the high gain (the imaginary part of the  $n_p$  as  $\text{Im}[n_p] = -1$ ) excites the broad dipolar FR, which reduces the peak of the OSF and results in the oblate and small negative force in broad radius range (the black solid curve). On the contrary, the low gain ( $\text{Im}[n_p] = -0.1$  and  $-0.01$ ) excites the high-order FRs with sharper profile and favors the sharper and larger negative force in different radius ranges (red dashed and blue dotted curves). However, the further increase or decrease of the gain ( $\text{Im}[n_p] = -2$  or  $-0.001$ ) suppresses completely the negative force [not given in Fig. 8(d) because of no occurrence of the negative force in the two cases]. In a word, only the appropriate gain can cause the negative OSF, while a too high or too low gain is disadvantageous for the generation of the negative OSF. On the other hand, other laser beams such as a Bessel beam can also cause negative OSF [35,36], but this goes beyond the range of the text.

## V. CONCLUSIONS

In summary, we have studied in theory the effects of the multipolar FRs with different types on the OSF upon a high-index dielectric nanoparticle impinged by a linearly polarized plane EM wave in the visible range. Our results

show unambiguously that the OSF can be decomposed into five components which correspond respectively to five types of multipolar FRs with different physical mechanisms. The magnetic (electric)-based cascades of FRs come from the interference between the scattered fields re-emitted by the electric (magnetic) multipole moments excited in the particle and background. They contribute mainly to the peaks of the OSF and exhibit the interplays between the scattered and incident fields. The magnetic (electric)-based conventional FRs come from the interference between the scattered fields re-emitted by the adjacent two-order electric (magnetic) multipole moments. The unconventional FRs emerge from the interference between the scattered fields reradiated by the same-order electric and magnetic multipole moments. The latter three types of FRs denote the rich electric and/or magnetic interactions between the scattered fields and can ruin the OSF’s peak for particular large nanoparticle. The superposition of all types of FRs causes the broad dips of the OSF and even near-zero force effect at particular radii. Surprisingly, various types of multipolar FRs arise in the same OSF and are expressed in a unified way. Furthermore, we derive the analytic formulae to calculate the particle radius at the peaks and dips of the OSF based on the FR’s conditions of the scattered field. The results agree well with that calculated by the rigorous Mie scattering theory. It illuminates quantitatively the effects of the FRs on the OSF. By comparing the OFSSs on the nanoparticles with different refractive indexes, the result shows that the negative OSF arises only for the particle with appropriate gain under radiation of a plane EM wave. Because of the strong magnetic and electric responses of the high-index dielectric nanoparticle, the peaks of the FRs can be employed to realize the large OFS under the illumination of the low-power laser beam. It is advantageous to reduce the heat effects of the laser and the thermal motion of the optically controlled nanoparticle. Additionally, the near-zero force effect caused by the dips of the FRs is advantageous to design the recoilless optical microscopy techniques. Our results are favorable not only for deep understanding of FRs in OSF but also for stable optical manipulation of the dielectric nanoparticle.

## ACKNOWLEDGMENTS

The authors are grateful to Professor Zhi-Fang Lin and Assistant Professor Nan Zhao for the reading of the manuscript

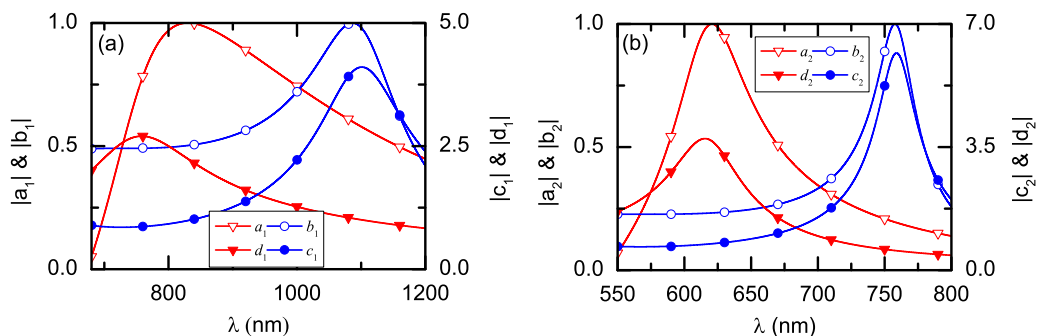


FIG. 9. The models of scattering coefficients  $a_l$  (red curves with hollow triangles) and  $b_l$  (blue curves with hollow circles), corresponding to the left axis, and internal coefficients  $d_l$  (red curves with solid triangles) and  $c_l$  (blue curves with solid circles), corresponding to the right axis, as functions of incident wavelength ( $\lambda$ ) when  $l = 1$  (a) and 2 (b). The particle radius is  $R = 130$  nm and the relative refractive index  $n = n_p/n_m = 4/1.33$ .

and valuable comments. The authors acknowledge financial support from National Natural Science Foundation of China (Grant No. 11174222).

#### APPENDIX: RELATIVE SHIFTS OF THE PEAKS OF $|a_l|$ ( $|b_l|$ ) WITH RESPECT TO THE PEAKS OF $|d_l|$ ( $|c_l|$ )

The peaks of  $|a_l|$  shift to the red side with respect to the peaks of  $|d_l|$  with  $l = 1$  and 2 as shown by the red curves with hollow triangles and with solid triangles in Figs. 9(a) and 9(b). On the other hand, the peaks of  $|b_l|$  shift to the

blue side with respect to the peaks of  $|c_l|$  with  $l = 1$  and 2 as shown by the blue curves with hollow circles and with solid circles in Figs. 9(a) and 9(b). Generally, except for the dipole ( $l = 1$ ) and quadrupole ( $l = 2$ ), the same phenomena also occur in higher-order moments such as octupole ( $l = 3$ ), hexadecapole ( $l = 4$ ), etc. But the relative shifts of the peaks became very small with further increase of the order of the moment (not given in the Fig. 9). Here the incident wavelength ( $\lambda$ ) is regarded as a variable and serves as horizontal axis in Fig. 9 to show clearly the red or blue shifts among the peaks. The particle with fixed radius  $R = 130$  nm and refractive index  $n_p = 4$  is immersed in water ( $n_m = 1.33$ ).

- 
- [1] D. G. Grier, *Nature (London)* **424**, 810 (2003).  
 [2] O. M. Marago, P. H. Jones, P. G. Gucciardi, G. Volpe, and A. C. Ferrari, *Nat. Nanotechnol.* **8**, 807 (2013).  
 [3] K. Dholakia and P. Zemanek, *Rev. Mod. Phys.* **82**, 1767 (2010).  
 [4] A. Ashkin and J. M. Dziedzic, *Appl. Phys. Lett.* **19**, 283 (1971).  
 [5] A. Ashkin, *Phys. Rev. Lett.* **24**, 156 (1970).  
 [6] Z. Yan, M. Sajjan, and N. F. Scherer, *Phys. Rev. Lett.* **114**, 143901 (2015).  
 [7] J. Ng, Z. F. Lin, C. T. Chan, and P. Sheng, *Phys. Rev. B* **72**, 085130 (2005).  
 [8] Z. Yan, R. A. Shah, G. Chado, S. K. Gray, M. Pelton, and A. N. F. Scherer, *ACS Nano* **7**, 1790 (2013).  
 [9] M. Nieto-Vesperinas, J. Sáenz, R. Gómez-Medina, and L. Chantada, *Opt. Express* **18**, 11428 (2010).  
 [10] B. Luk'yanchuk, N. I. Zheludev, S. A. Maier, N. J. Halas, P. Nordlander, H. Giessen, and C. T. Chong, *Nat. Mater.* **9**, 707 (2010).  
 [11] A. I. Kuznetsov, A. E. Miroshnichenko, Y. H. Fu, J. Zhang, and B. Luk'yanchuk, *Sci. Rep.* **2**, 492 (2012).  
 [12] Z. Li, S. Zhang, L. Tong, P. Wang, B. Dong, and H. Xu, *ACS Nano* **8**, 701 (2014).  
 [13] T. Cao, L. Mao, D. Gao, W. Ding, and C.-W. Qiu, *Nanoscale* **8**, 5657 (2016).  
 [14] T. Cao, J. Bao, L. Mao, T. Zhang, A. Novitsky, M. Nieto-Vesperinas, and C.-W. Qiu, *ACS Photon.* **3**, 1934 (2016).  
 [15] H. Chen, S. Liu, J. Zi, and Z. Lin, *ACS Nano* **9**, 1926 (2015).  
 [16] Y. Yang, L. Jiafang, and L. Zhi-Yuan, *J. Opt.* **17**, 075004 (2015).  
 [17] A. I. Kuznetsov, A. E. Miroshnichenko, M. L. Brongersma, Y. S. Kivshar, and B. Luk'yanchuk, *Science* **354**, 2472 (2016).  
 [18] M. V. Rybin, D. S. Filonov, P. A. Belov, Y. S. Kivshar, and M. F. Limonov, *Sci. Rep.* **5**, 8774 (2015).  
 [19] X. Kong and G. Xiao, *J. Opt. Soc. Am. A* **33**, 707 (2016).  
 [20] M. I. Tribelsky and A. E. Miroshnichenko, *Phys. Rev. A* **93**, 053837 (2016).  
 [21] M. V. Rybin, K. B. Samusev, I. S. Sinev, G. Semouchkin, E. Semouchkina, Y. S. Kivshar, and M. F. Limonov, *Opt. Express* **21**, 30107 (2013).  
 [22] M. I. Tribelsky, A. E. Miroshnichenko, and Y. S. Kivshar, *Europhys. Lett.* **97**, 44005 (2012).  
 [23] T. J. Arruda, A. S. Martinez, and F. A. Pinheiro, *Phys. Rev. A* **87**, 043841 (2013).  
 [24] T. J. Arruda, A. S. Martinez, and F. A. Pinheiro, *Phys. Rev. A* **92**, 023835 (2015).  
 [25] P. Debye, *Ann. Phys.* **335**, 57 (1909).  
 [26] C. F. Bohren and D. R. Huffman, *Absorption and Scattering of Light by Small Particles* (Wiley, New York, 1983).  
 [27] A. Rahimzadegan, R. Alaee, I. Fernandez-Corbaton, and C. Rockstuhl, *Phys. Rev. B* **95**, 035106 (2017).  
 [28] I. T. Michael, *Europhys. Lett.* **104**, 34002 (2013).  
 [29] A. B. Evlyukhin, S. M. Novikov, U. Zywietz, R. L. Eriksen, C. Reinhardt, S. I. Bozhevolnyi, and B. N. Chichkov, *Nano Lett.* **12**, 3749 (2012).  
 [30] J.-M. Geffrin, B. García-Cámara, R. Gómez-Medina, P. Albella, L. Froufe-Pérez, C. Eyraud, A. Litman, R. Vaillon, F. González, and M. Nieto-Vesperinas, *Nat. Commun.* **3**, 1171 (2012).  
 [31] I. Liberal, I. Ederra, R. Gonzalo, and R. W. Ziolkowski, *Opt. Express* **22**, 8640 (2014).  
 [32] P. C. Chaumet and A. Rahmani, *Opt. Express* **17**, 2224 (2009).  
 [33] A. Mizrahi and Y. Fainman, *Opt. Lett.* **35**, 3405 (2010).  
 [34] K. J. Webb and Shivanand, *Phys. Rev. E* **84**, 057602 (2011).  
 [35] J. Chen, J. Ng, Z. Lin, and C. Chan, *Nat. Photon.* **5**, 531 (2011).  
 [36] A. Novitsky, C.-W. Qiu, and H. Wang, *Phys. Rev. Lett.* **107**, 203601 (2011).